

RESEARCH

Open Access



# Seismic Performance of Precast Concrete Columns with Improved U-type Reinforcement Ferrule Connections

Zhiwu Yu<sup>1,2,3</sup>, Xiaoyong Lv<sup>1</sup>, Yujie Yu<sup>1,3\*</sup>, Faxing Ding<sup>1,3</sup> and Xiaodan Peng<sup>1</sup>

## Abstract

This paper proposes a new kind of U-type reinforcement ferrule (URF) connection for the assembly of precast concrete (PC) components, which has a good fault-tolerance ability and low cost of construction with a simple post-grouting process. The modified connection features welded U ferrules, which can increase the bonding mechanism and internal stress transmission in the spliced region. A series of quasi-static cyclic tests were performed on URF-connected PC columns with different welding patterns. Comprehensive comparisons were performed on the load-bearing capacity, the plastic energy dissipation ability, the internal force transmission, the column ductility and the stiffness. The results indicated that PC columns with welded URF connections can ensure better lateral resistance than the cast-in-place concrete column. The weld type and length influence the connection performance, and the 15d-welded and full-length welded URF connections presented better connection performance and were suggested for the assembly of PC columns. Then, finite element analyses were performed to further reveal the working and failure mechanisms and the affecting mechanism of some working parameters. Parametric simulations indicated that the increase in the axial load ratio and the concrete strength in the postcast region had a slight but limited effect on improving the lateral resistance of the column connection.

**Keywords:** U-type longitudinal reinforcement ferrule connections, prefabricated concrete column, lateral resistance, seismic behavior, finite element analysis

## 1 Introduction

Due to the advantages of high construction efficiency, low environmental pollution and flexible space arrangement, precast concrete (PC) structures have received considerable attention and have been widely adopted in structural engineering (Elliott 2016). Unlike traditional cast-in-place (CIP) concrete structures, PC structures have concrete elements prefabricated in a factory. These precast columns and beams are then connected on site with only a small amount of concrete casting or grouting work. Therefore, the main challenge facing the PC structures is the structural integrity, and the lap-splicing connection is

the crucial part. Although the PC construction method has been widely applied to various construction fields, the majority of studies have mainly been around the application of conventional joint details to evaluate the PC structures or the performance of the grouting materials. The development of enhanced joint details is still limited (Kim and Lee 2019). However, previous reports indicated that the majority of failures of PC structures in large earthquakes mainly came from insufficient ductility and quick damage accumulation at the joints (Mitchell et al. 1995; Gulkan 1998; Park 2002). Therefore, a favorable lap-splicing connection for PC structures requires not only a convenient construction method in the nature of prefabricated construction but also good seismic performance with enough stiffness, strength and good ductility (Choi et al. 2013).

At present, the sleeve connection is the most common method for the lap-splicing of longitudinal

\*Correspondence: yujiecsu@csu.edu.cn

<sup>1</sup> School of Civil Engineering, Central South University, Changsha 410075, China

Full list of author information is available at the end of the article

Journal information: ISSN 1976-0485 / eISSN 2234-1315

reinforcements, and the mechanical behaviors and the application operations have been extensively investigated. Tullini and Minghini (2016) tested grouted sleeve connections with the corrugated sleeves being positioned along the sides of the column cross section rather than at the corners. Experimental evidence indicated that this connection was effective in terms of ultimate limit state capacity. Belleri and Riva (2012) investigated the suitability of grouted sleeve connections as the column-to-foundation connections for PC structures in seismic regions. The results indicated that the grouted sleeves could ensure similar ductility and energy dissipation capacity of the structural members. Ou et al. (2009) proposed a combined connecting method with unbonded posttensioned tendons and bonded mild steel bars with sleeves. Test results showed that the proposed construction method can effectively transfer the internal stress and can ensure the ductility and energy dissipation ability of the precast columns. Sayadi et al. (2014, 2015) studied the bonding behavior of spliced sleeves located in the elastic and inelastic segments of the splice sleeves through bending tests on the assembled beams. It was found that providing an interlock mechanism in the elastic segment of the

sleeve would decrease the bond strength of the spliced sleeves and the load-carrying capacity of the beam.

Sleeve connections are proved to be an efficient and strong connecting method for PC structures and have gradually become the mainstream connections for PC structures (Wu et al. 2016). However, this connection still possesses many difficulties in practice, such as alignment difficulties and inconvenient detection of compactness for grouting (Fig. 1a). Therefore, except for those mechanical property investigations on extruded or grouted sleeve connections, many studies have also sought to find advanced connecting methods and more convenient construction approaches for PC connections. Hu et al. (2017), Nzabonimpa and Hong (2018) once proposed a novel PC-based dry mechanical joint with detachable metal slabs for column-to-column moment connection. In the proposed connections, a pair of steel plates was provided and connected by high-strength bolts to transfer the axial load and moment. Park et al. (2014) proposed a hybrid precast frame that incorporated a steel core at the joint region; then, the vertical reinforcements at the vertical splicing region can run into the steel cores for connecting. Smith et al. (2010, 2012) performed an

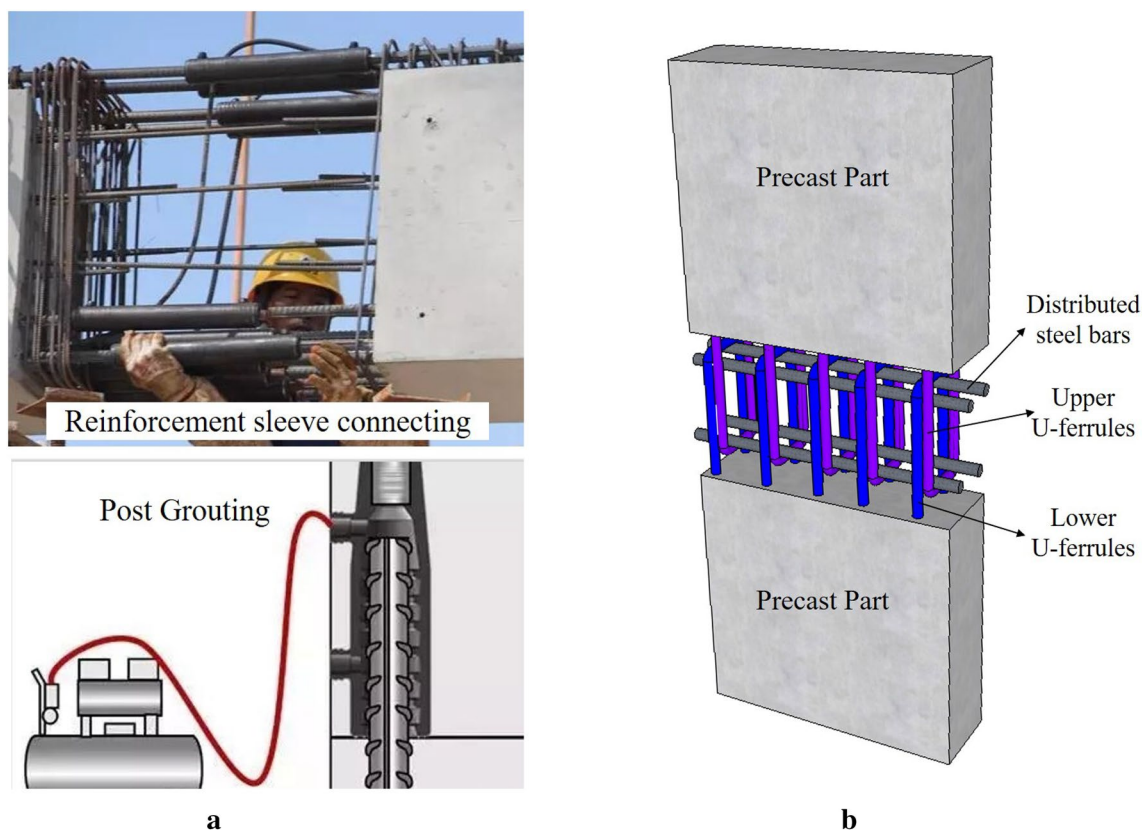


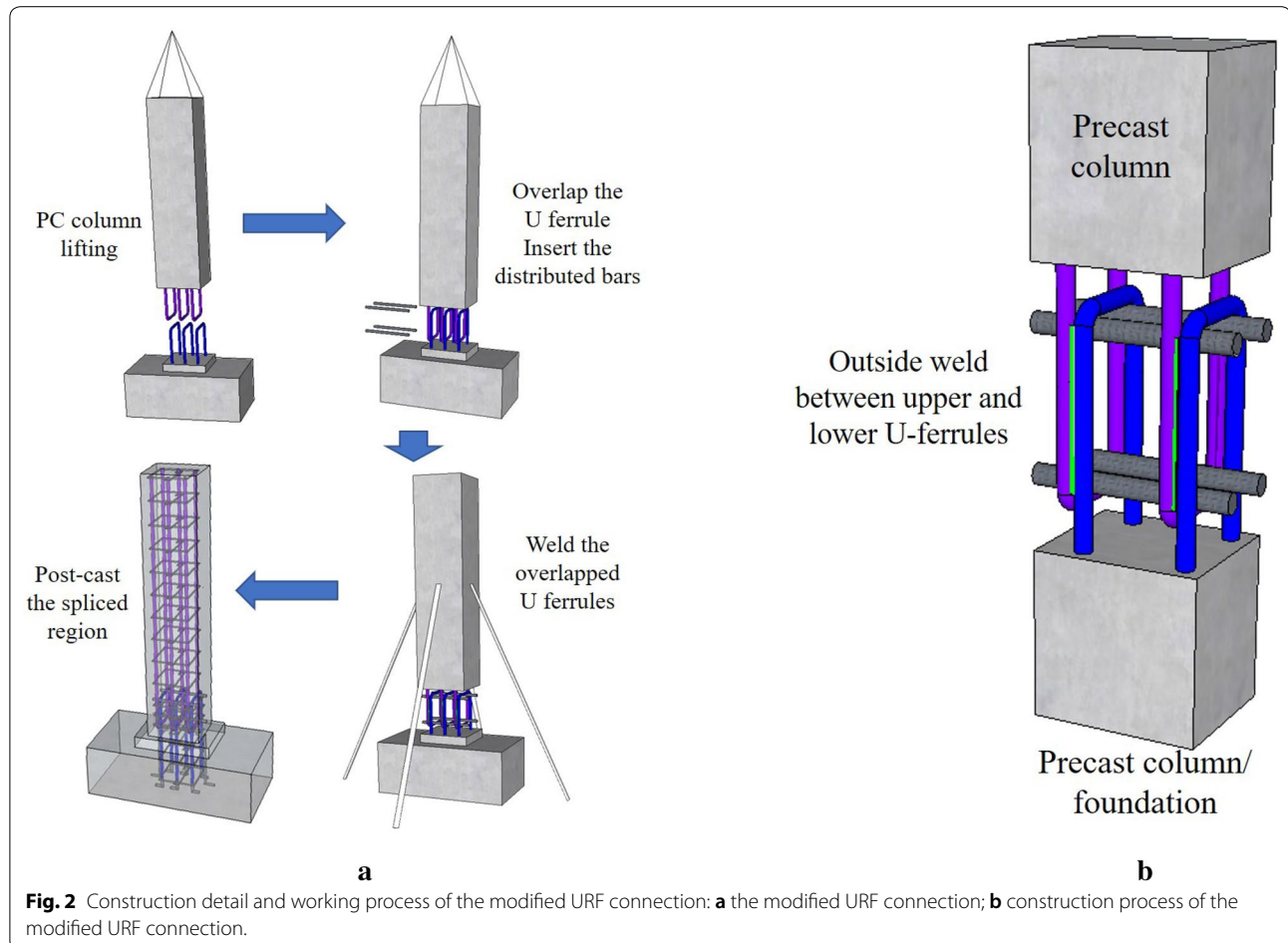
**Fig. 1** Construction details of the grouted sleeve connection and previous U-type reinforcement ferrule connection: **a** the grouted sleeve connection; **b** the U-type reinforcement ferrule connection.

experimental study on a hybrid precast concrete wall that was assembled with a combination of mild steel and high-strength unbonded posttensioning strands.

Recently, Yu et al. (2015a, b) put forward a new kind of U-type reinforcement ferrule (URF) connection (Fig. 1b) for the assembly of PC components. In this connection, the longitudinal reinforcements of the PC members were extended out and made into a U-type ferrule. In the connection of vertical PC components, the U-type ferrule of the upper and bottom PC members overlapped with each other. The distributed reinforcements were inserted through the corners of the U-shaped rings, forming the clamping mechanism between the reinforcements of the connected parts. This overlapping region was then filled with concrete on the construction site. Therefore, there is only a small amount of concrete grouting work at the connecting region, and the overall connection has a good fault-tolerance ability and a low cost of construction as well as a simple operational process. An experimental test was applied to the PC shear wall system assembled with the URF connections, and the pseudo static tests

indicated that the prefabricated shear wall can produce similar load-bearing capacity and seismic performance in comparison to those of the CIP shear walls. However, since the longitudinal reinforcements only overlapped with each other and the internal forces were simply transferred through the mechanical clamping effect of distributed steel bars, the spliced part would quickly lose the bonding mechanism once the post pouring concrete got crushed. Then, this connection presented weaker energy dissipation ability than traditional CIP shear walls (Yu et al. 2015a, b).

However, this URF connection presented a simple connecting idea for PC structures, and the main deficiency comes from the weak connection between the spliced U-type ferrules. Therefore, in this study, a modified connection detail was proposed to improve the internal force transmission and integration of the URF connection. The construction of the modified URF connection is given in Fig. 2a. The exposed U-type longitudinal reinforcement ferrules were welded together after being overlapped with each other, and the distributed steel bars



were also supplemented in the U-shape ring. In this way, the longitudinal reinforcements were bonded together to strengthen the internal force transmission, increasing the connection integrity. The modified URF connection still possesses a simple connecting and construction process, as shown in Fig. 2b. On the construction site, the PC columns can be lifted above the desired location and be positioned to overlap the U-ferrules conveniently. Then, the distributed steel bars are installed at the corner positions. The spliced U-ferrules are welded together before the concrete is cast at the splicing region. The PC column can be self-supported through the welded U-ferrules. Then, the need for lifting or supporting work is limited, and the compactness of the spliced region is easily ensured.

In this paper, this improved URF connecting method was applied to the assembly of PC columns, and a series of quasi-static cyclic tests were performed to investigate the connecting ability and seismic performance of the modified URF connections. Different parameters, such as welding method and welding length, were considered, and the traditional cast-in-place column and the PC column spliced with the grouted sleeve connection were also tested to compare the performance. Based on the test data, the optimal connection design and design suggestions were derived.

## 2 Experimental Study

### 2.1 Design and Fabrication of Specimen

The aim of the experimental tests was to investigate the performance of the modified URF connections and the optimum construction details. Therefore, a total of seven reinforced concrete column specimens were designed, including one CIP column as the reference BASE specimen, and six PC columns. The connection types and descriptions of the tested specimens are given in Table 1. Among the PC specimens, there was one previous version of the URF connection (no welding at the spliced U-shaped ferrules) and one specimen with an extruded sleeve connection. Four specimens with the modified

URF connecting method were designed with different welding methods and weld lengths. The test plan and specimens were designed based on the concrete design codes and testing standards (JGJ1-2014, 2014; JGJ/T101-2015, 2015). The connection details of each specimen are given in Fig. 3, and the setup plot versus the specimen design are given in Fig. 4.

The test specimens were designed into a PC column connecting to the PC base mode. The specimen constructions in the precast region remained the same, and only the assembly connecting methods changed within the 300 mm-high postcasting region. Both the PC base and the PC column had reserved 280 mm-high extruded U-ferrules for splicing and connecting. Similar to the construction process in Fig. 2a, the 1.2 m-long PC column was lifted above the base, and the upper and bottom U-ferrules were overlapped and welded together. For specimen ZP2, the PC parts were connected with extruded sleeve connections, and the extended reinforcements were aligned into the sleeves and clamped together through mechanical squeezing. After the connection of the reinforcements, the 300 mm-high connecting region was cast on-site.

The C30 concrete was used for the precast members and the CIP specimen (BASE). The design strength of C30 concrete is 14.3 MPa based on the concrete design code (JGJ1-2014, 2014), and this strength was used to determine the axial compression load. The self-compacting C35 concrete with a design compressive strength of 16.7 MPa was used for the postcast region. Before the test, the practical concrete compressive strength was obtained through the standard 150 mm cube test, and the obtained compressive strength was 32.67 MPa for the C30 concrete and 35.38 MPa for the C35 postcast concrete. These measured strengths were applied later in the finite element simulations and further studies. The boundary faces between the precast parts and the postcast region were scratched with 6 mm-deep nicks to create a rough surface for firm bonding. The HRB400 ribbed bars, with a characteristic yield strength of 400 MPa

**Table 1** Tested specimens and splicing methods.

Specimens	Splicing methods
BASE	Cast-in-place
ZP1	Previous URF connection
ZP2	Extrusion sleeve connection
ZP3	URF connection with 10d-long welding—identical position between two sides
ZP4	URF connection with 10d-long welding—staggered position between two sides
ZP5	URF connection with 15d-long welding—identical position between two sides
ZP6	URF connection with full-length welding

d refers to the diameter of U-type longitudinal reinforcement.

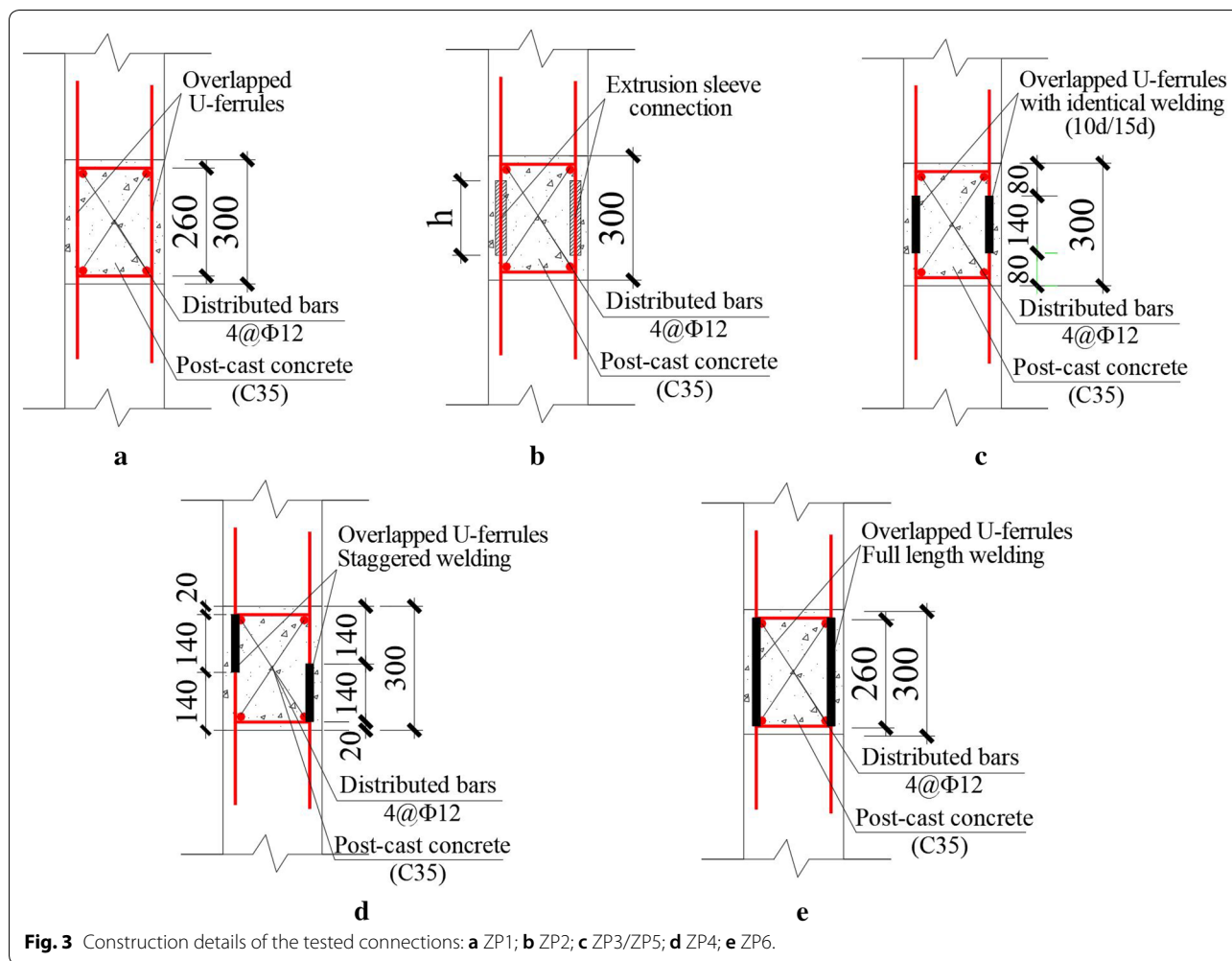


**Fig. 3** Construction details of the tested connections: **a** ZP1; **b** ZP2; **c** ZP3/ZP5; **d** ZP4; **e** ZP6.

and a characteristic ultimate strength of 540 MPa, were used for reinforcements and ferrules. The real mechanical properties of the steel bars were also measured with standard material tensile tests, and the detailed mechanical properties are given in Table 2.

**2.2 Experimental Program**

The tests were designed to investigate the seismic performance of the assembled connections at the foot of the column. All the specimens were tested as vertical cantilevers, and the quasi-static cyclic displacement load was applied at the top end, as shown in Fig. 5a. A constant axial load of 360.36 kN was applied with a hydraulic jack located at the top end of the column. The axial load was calculated based on the 0.3 axial compressive ratio and the designed compressive strength of the concrete column (the product of the design compressive strength of the C30 concrete and the section area of the column). The axial jack was against a reaction beam which can move horizontally with the top of the column, ensuring

the free end boundary at the top end. The horizontal displacement was applied at the top column end with a two-stage loading scheme, based on the “Specification for seismic testing of buildings-JGJ/T101-2015” in China (JGJ/T101-2015, 2015). First, the load-controlled loading process was adopted, under which the lateral load was applied to the top with a load increment of 1/2 of the predicted yield strength  $P_y$ . Once obvious stiffness reduction appeared, the specimen was regarded as yielded, and the applied load and applied displacement at the yielding moment were obtained as  $F_\Delta$  and  $\Delta$ , respectively. Then, the loading method was shifted to displacement control with the practical yielding displacement  $\Delta$ . During the first loading stage, each cycle was repeated once, while in the second displacement-controlled stage, each loading amplitude was repeated twice. The test was terminated when the specimen displayed abrupt failures or the lateral resistance decreased below 85% of the maximum capacity. The loading protocol is given in Fig. 5b. By using this loading protocol, the yield load, the nonlinear deforming

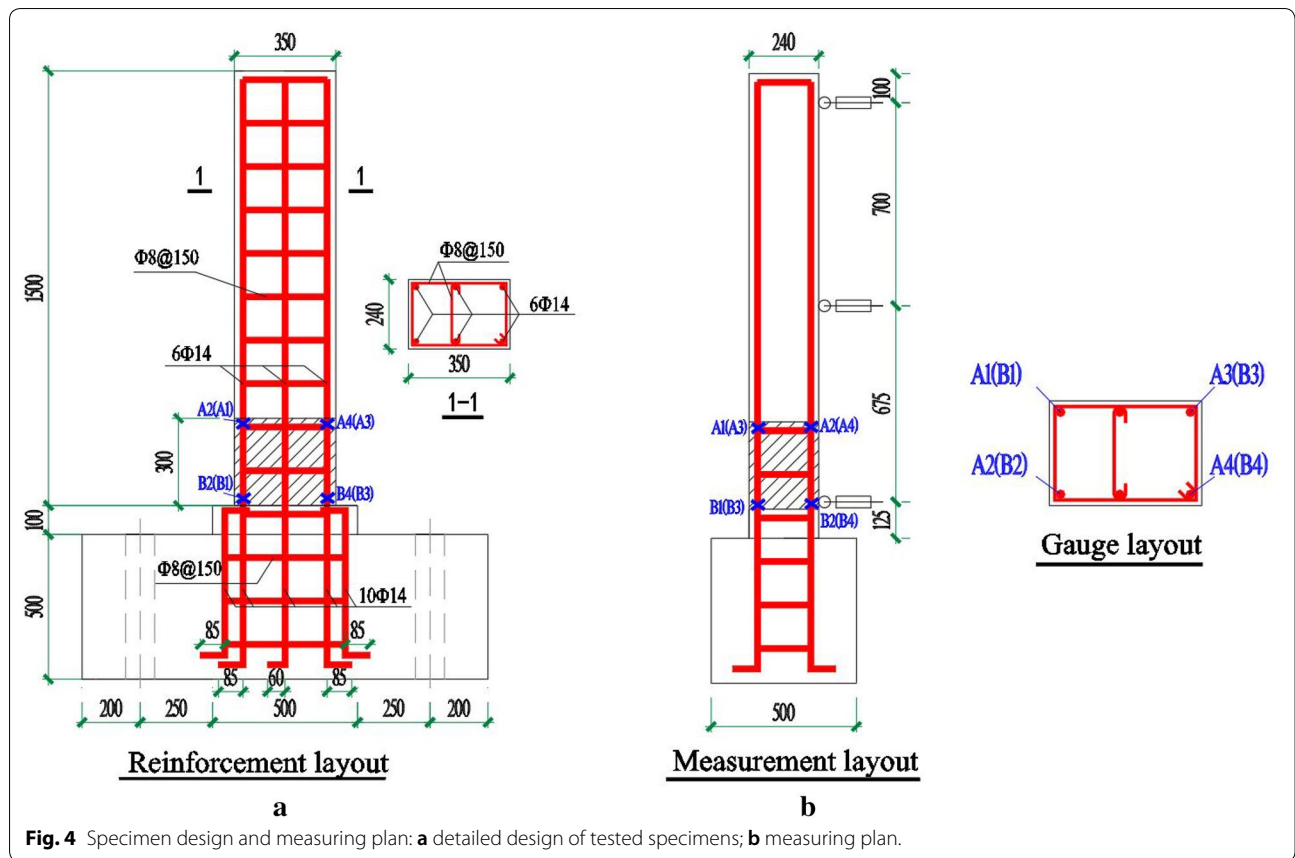


**Fig. 4** Specimen design and measuring plan: **a** detailed design of tested specimens; **b** measuring plan.

**Table 2** The measured mechanical properties of the steel bars.

Reinforcement type	Diameter (mm)	Elastic modulus (MPa)	Yield strength $f_y$ (MPa)	Ultimate strength $f_u$ (MPa)	Elongation (%)
HRB400	8.0	$2.03 \times 10^5$	520.8	656.3	28.2
HRB400	14.0	$1.97 \times 10^5$	441.7	558.1	30.1

ability and the ductility behaviors can be conveniently reflected through the obtained hysteretic curves.

### 2.3 Measuring Plan

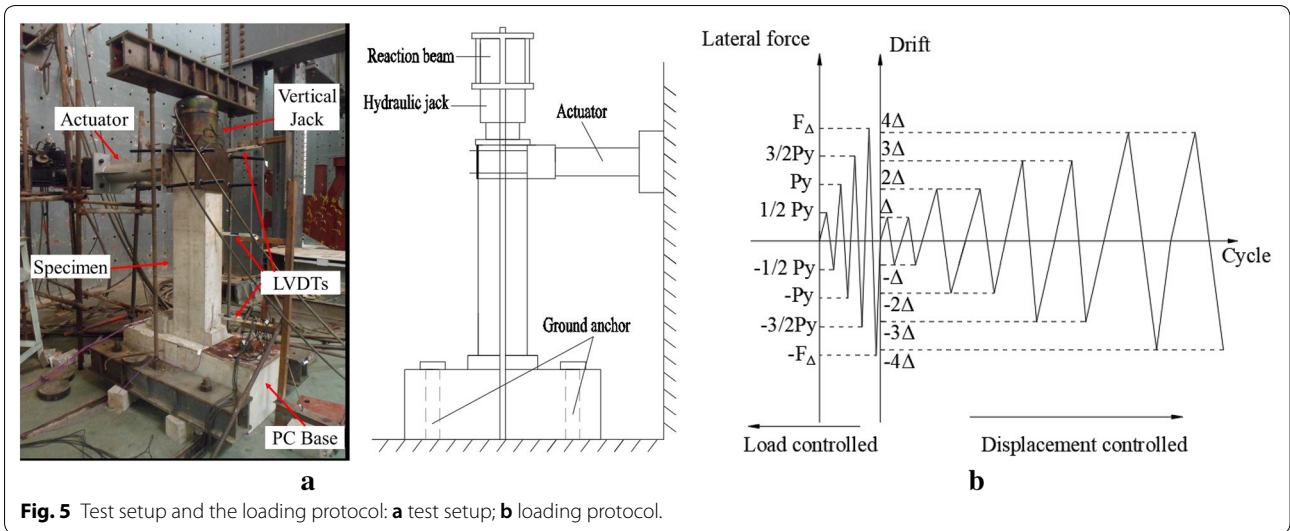
During the test, the failure behaviors and the crack developments were mainly recorded through visual observations. The applied horizontal load and the vertical load were recorded through a load sensor. During the test, the strain developments at the steel reinforcements were recorded through preinstalled strain gauges. The strain gages of the CIP BASE specimen were arranged on four longitudinal reinforcing bars (B1–B4) at the position of 20 mm high above the concrete base, as shown in Fig. 4b. The strain gauges of the assembled specimen ZP1–ZP6 were arranged on both sides of the four corner

longitudinal bars. Similarly, four pairs of strain gauges (B1–B4) were installed at the root of the bottom U-ferrules at a height of 20 mm above the base. Another four pairs of strain gauges (A1–A4) were installed at the root of the upper U-ferrules at a height of 280 mm above the base. Displacement meters were horizontally mounted at the top, middle height, and bottom end of the column to obtain the deformation pattern of the column during the test (Fig. 4b).

## 3 Test Results and Discussion

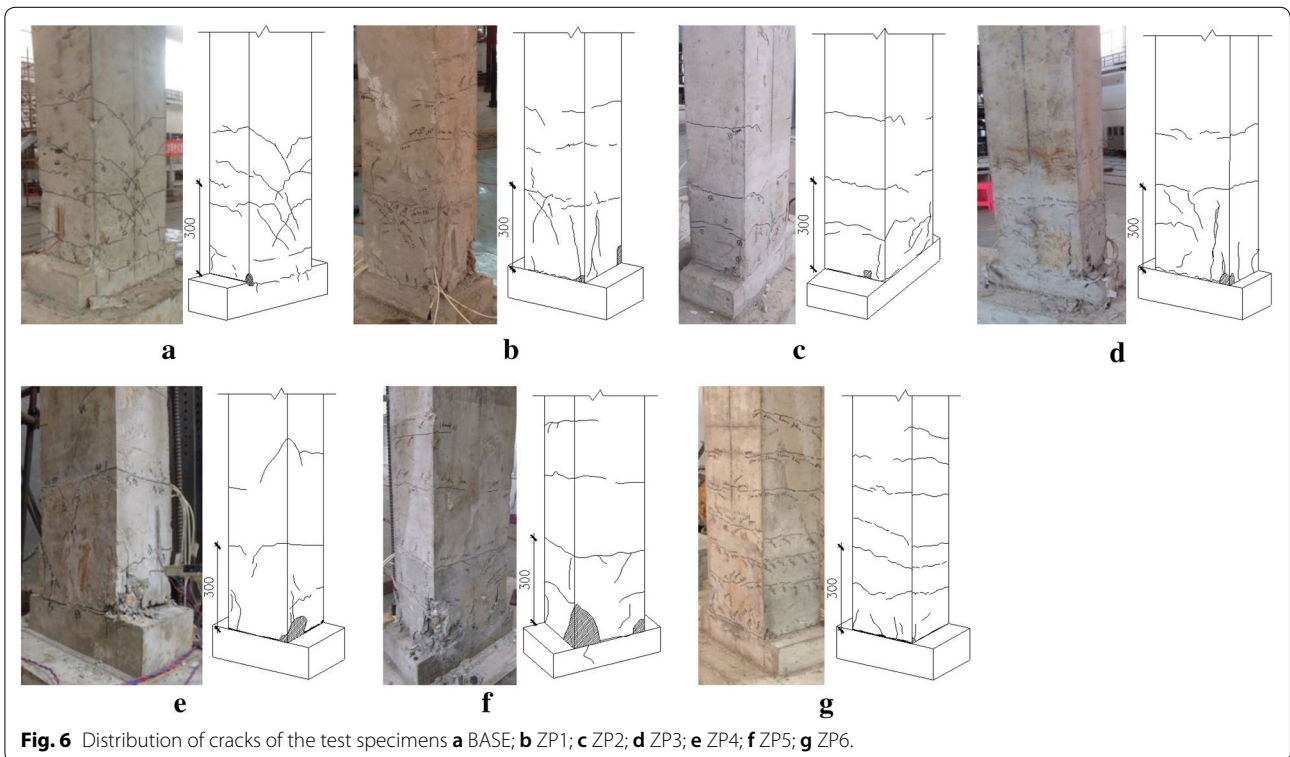
### 3.1 Failure Modes

The tested specimens all displayed a failure pattern that was similar to the small eccentric compression failure of the reinforced concrete column. The compressive steel



bars generally yielded ahead of the tensile bars, and the margin concrete on the compression side reached the compressive strength earlier than the compressive bars. The damage stage and the crack distributions at the end of the test are given in Fig. 6. The horizontal concrete cracks at the column root location initiated ahead of the appearance of the stiffness degradation of the specimen. Once the specimen yielded, those horizontal cracks

propagated quickly and went oblique. As the amplitude of the lateral displacement increased, the cracks at the upper and bottom boundaries of the postcast region gradually penetrated the postcast parts. During the large lateral displacement cycles, the concrete region on the tension side displayed wide cracks, and the column root on the compression side was crushed with regional concrete spalling. During the last few cycles before failure,



some longitudinal bars buckled and bulged out, and then the specimens could no longer provide resistance to the lateral load.

Different connection details also presented a certain influence on the crack distributions. In the CIP column, the concrete cracks firstly initiated at the column root and then evenly spread along the bottom half range of the column with oblique crossing cracks. This crack distribution indicated the good integrity of the column and a uniform stiffness along the column. For the column with the previous URF connection (ZP1), the cracks and concrete failure also started from the column roots. As the lateral load increased, more cracks appeared, but the cracks were mainly horizontal, and the majority of the cracks were concentrated at the upper boundary between the PC part and the postcast part. This cracking mode indicated that the boundary surface was a weak spot. Therefore, through-cracks were formed across the boundary sections early, and the concrete at the column corner crushed early. Moreover, considerable diagonal cracks formed later, which started from the crushed corner and then propagated to the boundary surface level. When the diagonal cracks connected the horizontal through cracks, the column displayed obvious lateral strength degradation and then failed quickly. Similar cracking and failure modes were also observed during the test of specimen ZP3. However, specimens ZP4 and ZP5 had different cracking modes. Fewer diagonal cracks were observed, but there was a horizontal crack at the upper boundary level, and the horizontal crack came across the entire section. The column corners also displayed intense concrete crushing failure. However, the postcast region had limited cracks, especially in specimen ZP4. The concrete crushing was less prominent in specimens ZP2 and ZP6, which had grouted sleeve connections and fully welded URF connections, respectively. In specimen ZP2, the cracks were mainly distributed within the postcast region. The cracks in ZP6 were mainly horizontal and were evenly distributed along the column. From the point of view of the cracking and failure mode, specimen ZP6 had the best integrity.

### 3.2 Hysteretic Curve

Figure 7 gives the obtained lateral displacement versus lateral load hysteretic curves. The enclosed area of the hysteretic loops indicates the dissipated energy in the specimens; then, a plump hysteretic loop with a larger enclosed area is often expected in structural seismic design. In some previous experimental studies of reinforced concrete or precast concrete structures, the concrete connections often have pinched and narrow hysteretic loops due to the fracture failure of the concrete materials and the early debonding at the surface of

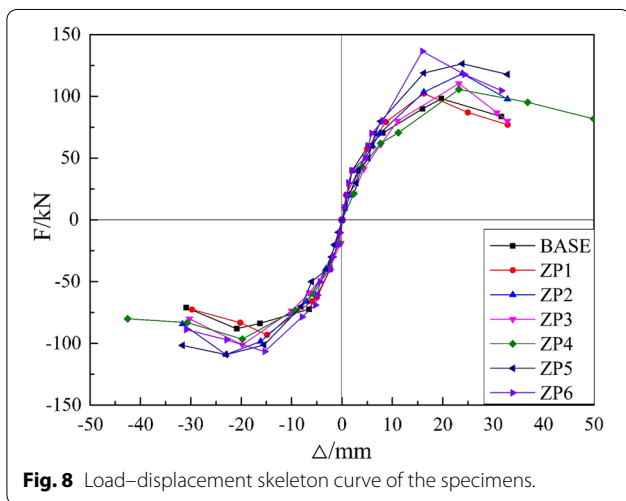
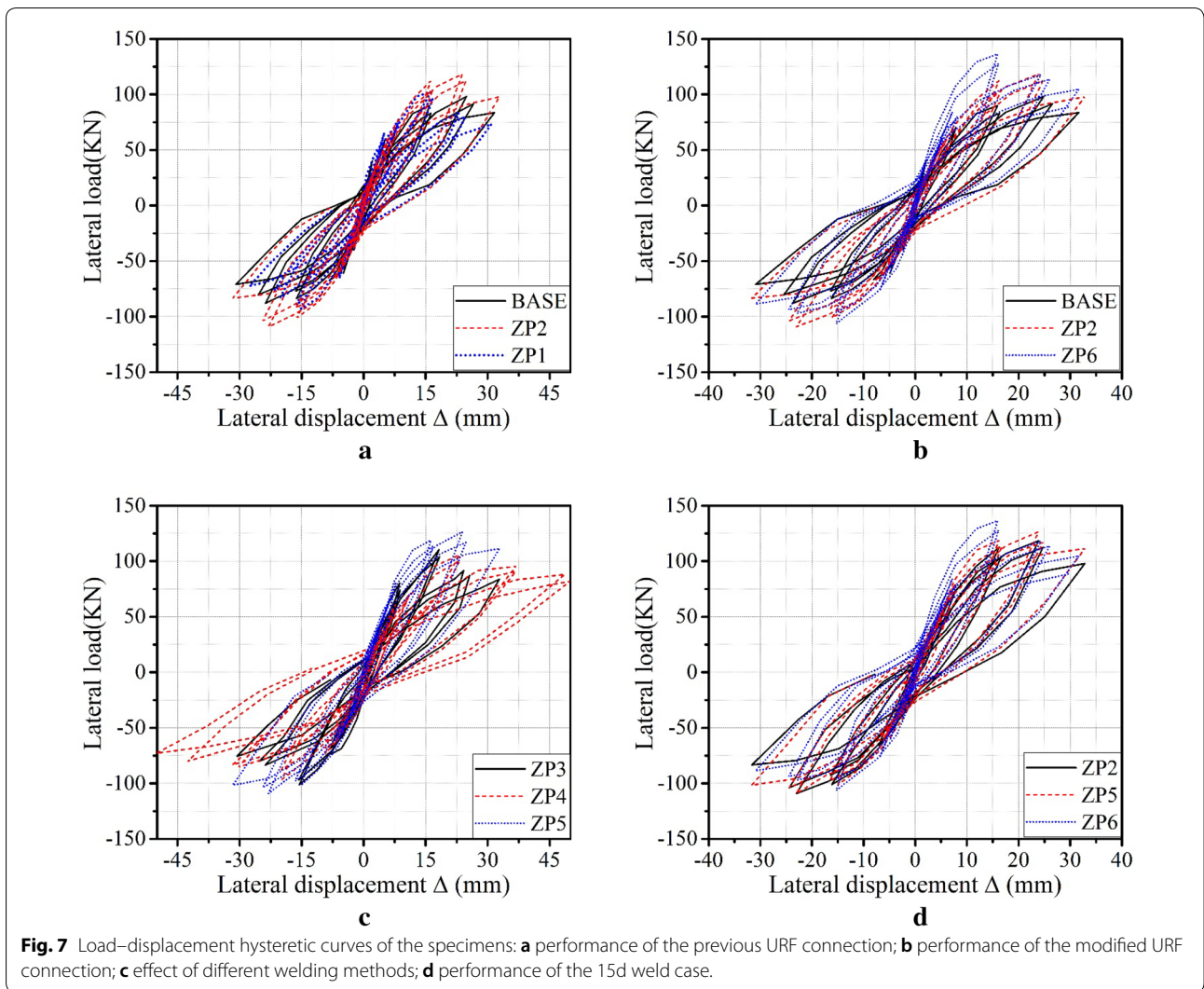
the reinforcements (Ghaye et al. 2017; José et al. 2018). In this study, the hysteretic curves of the tested CIP concrete column and precast specimens all displayed a comparatively plump shape, indicating a moderate energy dissipation ability. The slight pinching phenomenon was displayed for all tested specimens, which may mainly result from concrete cracking and the debonding of the reinforcing bars. As concrete crushing and longitudinal reinforcement buckling developed, the lateral stiffness of the specimens gradually decreased, and the residual deformation after unloading within each cycle gradually increased.

Figure 7a presents a comparison of the previous URF method connected column with the CIP column and the spliced sleeve-connected column. Figure 7b–d compares the modified URF connections. The results indicated that the sleeve connection could present strong bonding between the spliced longitudinal reinforcements, thus leading to the high lateral strength and stiffness of the assembled column. However, the PC column with a previous URF connection (ZP1) had a smaller lateral strength bearing ability than did the CIP column (BASE). This weak connecting ability was mainly attributed to the weak clamping mechanism between the spliced longitudinal reinforcements. The internal forces between two PC parts were transferred through only the concrete bonding and the mechanical clamping between the overlapped U-ferrules. When the overlapped U-ferrules were strengthened with full-range welds (ZP6), the lateral bearing strength of the PC column obviously increased, even surpassing the maximum capacity of the column with the sleeve connection (ZP2). Once the concrete crushed and reinforcements buckled, the lateral resistance degraded quickly, and afterward, the strength decay was similar to that of specimen ZP2.

Figure 7c compares the performance of the modified URF connections with different welding strategies. The two specimens with a 10d-long welds (ZP3 and ZP4) had similar lateral resistance, but the specimen with a staggered weld (ZP4) presented better deforming ability, leading to a good ductility and energy dissipation but relatively weak initial stiffness. Specimen ZP3 (10d identical weld) presented fast strength degradation after reaching the maximum capacity. The 15d weld case ZP5 had a higher lateral strength and better strength-retaining ability than ZP3. Moreover, the column with the 15d-welded URF connection presented similar lateral bearing performance to that of the column with the fully welded URF or the column with the extruded sleeve connection (Fig. 6d).

### 3.3 Load–Displacement Skeleton Curve

Figure 8 compares the skeleton curve of the tested specimens. The PC columns all displayed higher lateral



resistance and relatively higher initial stiffness than the CIP column. The concrete strength in the postcast region was higher than that of the CIP column. The construction of the spliced U-ferrules formed a double-reinforcement region. Then, the relatively stronger nature in the postcast region led to increased strength in the PC specimens. Since the previous URF connection had not ductile bonding between the spliced U ferrules, then the specimen presented weak ductility, leading to a fast strength degradation after concrete crushing and spalling. And the strength decay rate of previous URF connection specimen was similar to that of the CIP specimen. The modified URF connections ZP3 and ZP4 with short welds (10d staggered or identical) presented only limited ultimate strength increases but similarly displayed a fast strength decay rate when compared to those of the CIP BASE specimen. However, when the welding length was increased to the 15d or full length, the lateral bearing

strength of the column was improved dramatically. Specimen ZP6 had the maximum lateral strength, but the strength deterioration was also fast, showing an unstable strength-retaining ability. Thus, from the point of view of the strength level, strength-retaining ability and deforming ability, the 15d identical-welded case ZP5 possessed the optimum performance.

### 3.4 Critical Strengths and Ductility Performance

Throughout the loading process until failure, there were several critical conditions of the connections, which were the crack initiation state, the yielding state, the ultimate state and the failure state. The lateral resistance and deformation at those critical states were obtained, as shown in Table 3. The cracking loads of the PC columns were all slightly lower than that of the CIP column. The reason for this difference was the relatively weak interface bonding between the precast and postcast concrete, and early cracks mainly started from the lower boundary between the PC base and the postcast region. Due to the usage of higher-strength concrete in the postcast region, the PC columns all displayed higher yielding loads, peak loads and failure loads than the CIP column. Among all the PC columns, specimens ZP5 and ZP6 presented the maximum yielding and peak loads, indicating that the 15d-length welding and full-length welding measures can provide enough bonding and load transferring ability between spliced U-ferrules.

Ductility refers to the deforming ability of a structure or component without significant strength reduction, which is generally described with the ductility coefficient  $\mu = \Delta u / \Delta y$ . Here,  $\Delta u$  and  $\Delta y$  refer to the ultimate and yield displacements of the column, respectively. The ductility coefficient of each tested column is also given

in Table 3. The ductility coefficients of the PC columns with the modified URF connections were all larger than 3.92. The average coefficient for the CIP column was 3.77. While the specimen with a previous URF connection presented an average ductility coefficient of only 3.69, which was even smaller than that of CIP BASE specimen. This deficiency also revealed the weak bonding mechanism in the previous URF connection, when the U-ferrules were just overlapped with each other and were bonded through concrete bonding. The clamping mechanism will be degraded quickly under the concrete debonding and cracking behaviors, and the overlapped U-ferrules would have relative slipping or shifting, then leading to the early formation of a plasticity hinge and weak deforming ability. However, when the overlapped U-ferrules were welded together, the U-ferrules would form a kind of small frame mechanism within the post-cast region. The internal force can be transferred through the welded reinforcements. The U-ferrules can be firmly clamped before the weld failure. The ductility coefficient results proved that the modified URF connections with welded U-ferrules can effectively improve the cooperative working mechanism within the assembly connection. And the specimen ZP4 and ZP5 displayed the optimum deforming ability.

### 3.5 Internal Force Transferring-Ability at Reinforcing Steel Bars

The lateral strength and ductility performance indicated that the welded U-ferrules can improve the internal force transferring ability between spliced reinforcements. Then, to further validate the cooperative working mechanism between the spliced reinforcements, the strain gauge data were obtained and compared. During the

**Table 3** Strength and deformation extent at critical conditions.

No.	Loading direction	Cracking state		Yield state		Ultimate state		Failure state		$\mu$
		F/kN	$\Delta$ /mm	F/kN	$\Delta$ /mm	F/kN	$\Delta$ /mm	F/kN	$\Delta$ /mm	
BASE	+	45.6	3.82	65.0	8.36	93.6	24.81	83.6	31.62	3.78
	-	44.7	3.73	-63.8	-8.20	-83.1	-23.82	-71.0	-30.91	3.76
ZP1	+	39.8	3.43	70.3	8.20	102.3	16.22	77.1	32.81	3.96
	-	39.3	3.26	-65.7	-7.68	-93.0	-15.21	-83.0	-29.81	3.41
ZP2	+	41.3	3.03	70.3	7.82	118.3	23.91	97.8	32.82	4.37
	-	40.6	2.97	-66.1	-7.56	-109.1	-23.04	-84.3	-31.63	4.41
ZP3	+	40.3	3.06	72.3	8.36	110.5	18.22	83.7	32.80	3.92
	-	40.1	2.86	-69.2	-8.03	-101.1	-15.51	-75.6	-30.73	3.82
ZP4	+	39.2	3.68	70.6	11.2	105.6	23.13	81.8	49.90	4.46
	-	38.9	3.43	-68.9	-9.39	-96.5	-19.81	-80.2	-42.52	4.53
ZP5	+	41.5	3.07	75.8	7.58	126.3	23.91	111.3	32.81	4.98
	-	40.9	2.92	-73.6	-8.05	-109.1	-23.02	-101.5	-31.63	3.93
ZP6	+	42.3	3.26	78.6	7.92	136.5	15.90	104.6	31.70	4.00
	-	41.7	3.06	-76.6	7.62	-106.5	15.31	88.8	30.91	4.06

test, the strain conditions at the corner reinforcements were recorded to evaluate the internal force transmission performance of the splicing connections. As in Fig. 4b, the strain gauges were located at the column roots, the A gauges were mounted at the corner steel bars that extended from the PC column, and the B gauges were installed at the steel bars that extended from the base. Therefore, the strain difference between the A and B gauges can reflect the extent of the internal stress transfer through the spliced region. Here, the average strains of A1 with A2 and B1 with B2 were calculated as the strain representatives at the A and B locations (the strains are tension values under the positive loading direction).

The lateral load versus the measured strain relations at the A and B positions are given in Fig. 9. During the initial loading stage, the steel bars all had a linearly increased strain, and the strain developments in the PC columns were all similar to the strains at the same position in the CIP column. When the tested columns yielded, the strain levels in the PC columns all displayed a slower increase, and the strain levels were all lower than those at the same reinforcement positions in the CIP column. And this lower strain levels in PC column may mainly come from the increased area of reinforcements at the spliced region. And the enlarged reinforcements at spliced region also increased the mechanical bonding to the post-cast concrete, thus leading to more load transfer through the concrete part and then lower internal force transfer at the reinforcements. Moreover, the strain levels at the A and B locations started to present differences after column yielding, and the strains at the two positions also developed at different rates as the lateral load increased. This strain difference was large in ZP1, ZP3 and ZP4. Among the columns with the modified URF connections, the variation gaps between the A and B strains were small in ZP5 and ZP6 and in the sleeve-connected column ZP2.

The A and B strain differences could be used to calculate the strain loss rate at the spliced region, which was calculated as the ratio of the A–B difference to the strain level at spot A. The obtained results are given in Table 4, and the comparison indicated that the previous URF-connected column (ZP1) had relatively poor internal force transmission ability since the strain loss at different stages were all quite high. The reinforcements of specimens ZP2, ZP5 and ZP6 displayed less stress loss, which was approximately 10% when they reached the yield state and approximately 13% at the ultimate state. Therefore, the results in Table 4 indicated that the welding measure can effectively improve the coworking behaviors at the splicing region. Additionally, there was a minimum welding length to ensure sufficient bonding between the spliced bars, but the determination of the minimum length still need more experimental data.

### 3.6 Analysis of Stiffness Degradation

According to the specification for seismic testing of buildings (JGJ/T101-2015, 2015), the stiffness of the specimen can be expressed by the secant stiffness at each hysteretic loop with the following formula:

$$K_i = (|+F_i| + |-F_i|) / (|+X_i| + |-X_i|) \quad (1)$$

where  $F_i$  and  $X_i$  represent the peak resistance and applied displacement at cycle  $i$ . The stiffness degradation conditions are plotted in Fig. 10. The stiffness degrades quickly from the period of concrete cracking to column yielding. During this period, the stiffness of the BASE specimen had the fastest reduction. The PC specimens, except for ZP4, all displayed higher stiffness and slower stiffness degradation than the CIP column. After yielding, the lateral deformation of the column mainly came from the enlargement of the existing concrete cracks but with limited formation of new cracks. The plasticity development and strength hardening at the reinforcements could partly compensate for the strength reduction from the concrete degradation. Then, the stiffness degradation displayed a slight alleviation from yielding to the ultimate load period. Specimens ZP2, ZP5 and ZP6 displayed relatively higher stiffness levels and slower stiffness degradation rates, proving the good connecting performance of the sleeve connection, the 15d-welded and the full-welded URF connections.

### 3.7 Analysis of Energy Dissipation Ability

The energy dissipation ability of the test specimens can be evaluated with the equivalent viscous damping coefficient  $h_e$ , which is expressed as follows:

$$h_e = S_{ABCD} / 2\pi S_{(\Delta OBE + \Delta ODF)} \quad (2)$$

where  $S_{ABCD}$  is the area enclosed by the curve ABCD, and  $S_{(\Delta OBE + \Delta ODF)}$  is the sum of the area of the triangle OBE and ODF, as shown in Fig. 11. According to related studies (José et al. 2018), the concrete connections that fulfill the minimum requirement of the relative energy dissipation ratio (an index defined in ACI 374.1-05) presented an equivalent viscous damping coefficient  $h_e$  between 0.03 and 0.07, generally below or at approximately 0.1.

The equivalent viscous damping coefficients of the tested specimens are given in Table 5. As the applied lateral load increased, the equivalent viscous damping coefficient  $h_e$  gradually increased, representing the increased plastic energy consumption ability. In general, the equivalent viscous damping coefficient of the tested PC columns with the modified URF connection were similar to that of the CIP column, indicating that the PC columns can provide similar energy dissipation performance as the traditional CIP column. The

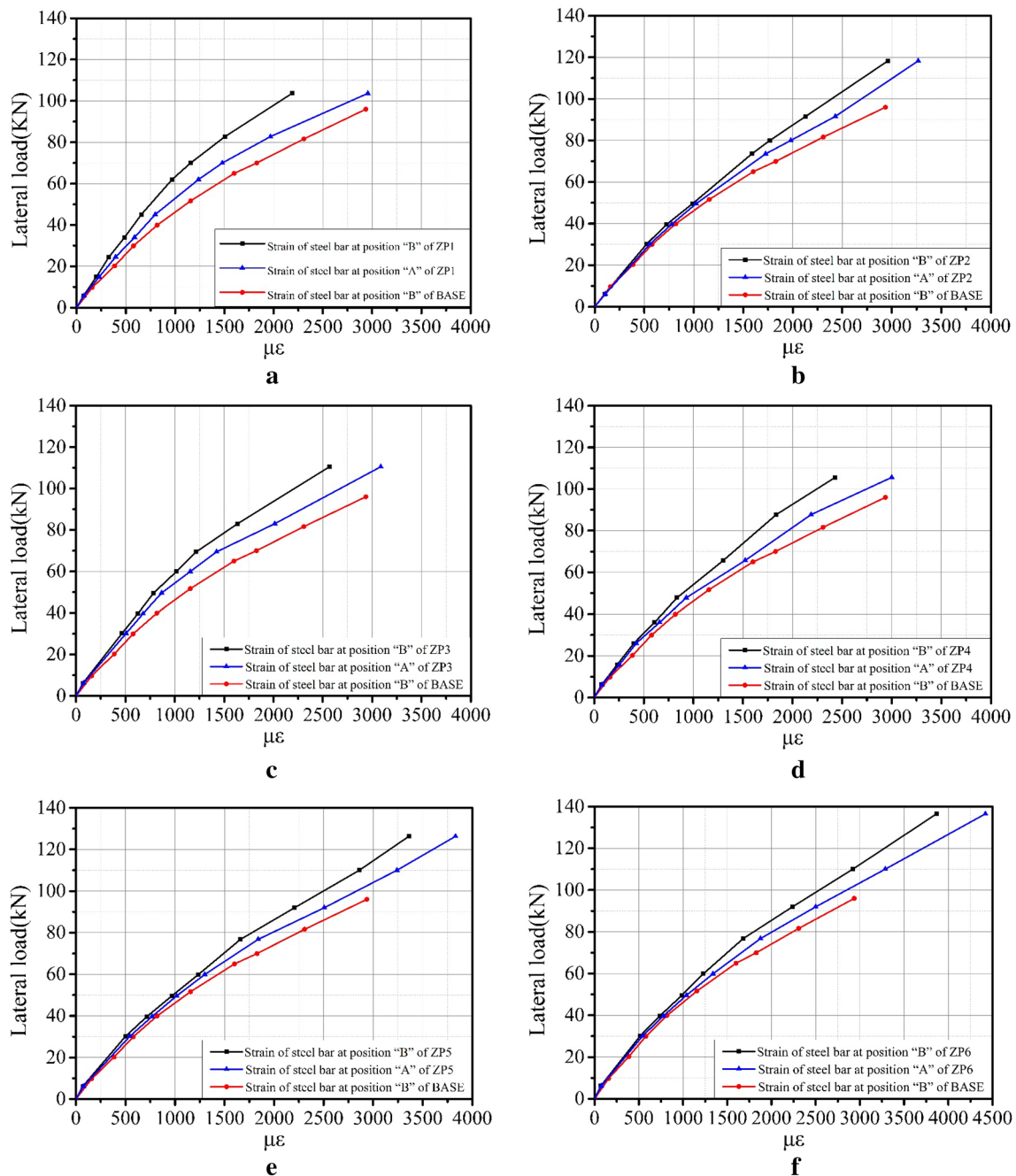


**Fig. 9** Load-strain curves of reinforcing bars at the A and B positions of the specimens: **a** ZP1; **b** ZP2; **c** ZP3; **d** ZP4; **e** ZP5; **f** ZP6.

maximum equivalent viscous damping coefficient  $h_e$  of the tested specimens all surpassed 0.1, and specimens ZP5 and ZP6 also displayed a relatively higher damping coefficient  $h_e$  than that of the CIP BASE specimen,

indicating a better energy dissipation ability. Then, from the test data and the above discussion, the PC columns with the modified URF connection needed at least 15d-length welding at the spliced ferrules.

**Table 4 Strain loss conditions of tested PC specimens.**

Case	ZP1 (%)	ZP2 (%)	ZP3 (%)	ZP4 (%)	ZP5 (%)	ZP6 (%)
Cracking state	13.0	3	11.4	12.3	6.63	7.5
Yield state	26.7	8.4	16.6	20.6	11.5	12.4
Ultimate state	32.6	10.7	21.4	24.3	14.3	13.5
Cracking state-yield state	13.7	5.40	5.20	8.3	4.87	4.90
Cracking state-ultimate state	19.6	7.70	10.0	12.0	7.67	6.00

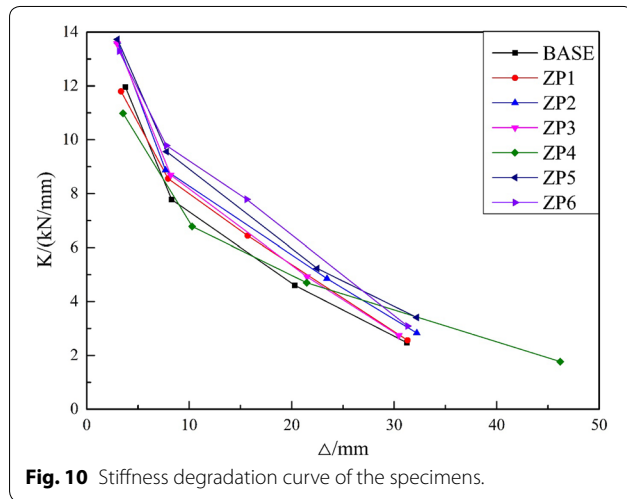


**Fig. 10** Stiffness degradation curve of the specimens.

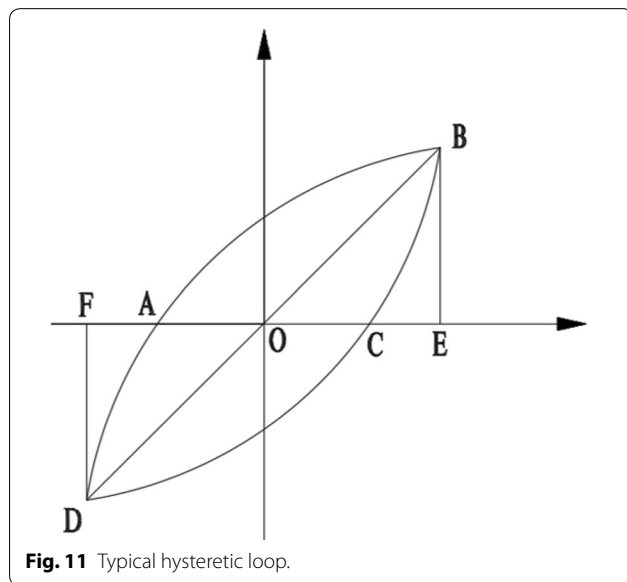


**Fig. 11** Typical hysteretic loop.

**4 Finite Element Analysis (FEA)**

**4.1 FEA Modelling**

To better understand the internal stress distribution and the damage propagation process, the corresponding finite element models of the tested specimens were

**Table 5 The equivalent viscous damping coefficient of the specimens.**

No.	The equivalent viscous damping coefficient $h_e$			
	$\Delta_y$	$2\Delta_y$	$3\Delta_y$	$4\Delta_y$
BASE	0.060	0.086	0.116	0.127
ZP1	0.047	0.067	0.097	0.107
ZP2	0.062	0.085	0.117	0.128
ZP3	0.055	0.080	0.111	0.121
ZP4	0.070	0.083	0.113	0.123
ZP5	0.078	0.092	0.119	0.138
ZP6	0.060	0.087	0.132	0.143

established with ABAQUS, as shown in Fig. 12. The eight-node 3D solid element with the reduced integral format (C3D8R) was used to model the concrete column. And the steel reinforcements were modeled with the truss element T3D2 which were embedded in the concrete to simulate the bonding relations between the steel bars and the concrete. Here the numerical model of specimen BASE, ZP1 and ZP6 were established. And the difference between the three models was the reinforcement modelling at the spliced region. In the BASE model, the longitudinal reinforcements were continuous from the column to the base. While for the PC column, the reinforcements were separated. In model ZP1, the reinforcement truss elements of PC column and the base were spliced and embedded with the same concrete part, but not connected. Since the U-ferrules in ZP6 were welded together, and the longitudinal reinforcement can be regarded as doubled at the spliced region. Therefore, in the numerical model, the reinforcement truss elements were also continuous but have double section area at the spliced region. Nodes at the bottom surface of the base was restrained at the three direction displacements to simulate the fixed end in the test. The nodes at the top end of the column were coupled to the center point where the axial constant force and lateral displacement load was applied, to simulate the free end loading boundary at the top column end. The analyses were solved with standard

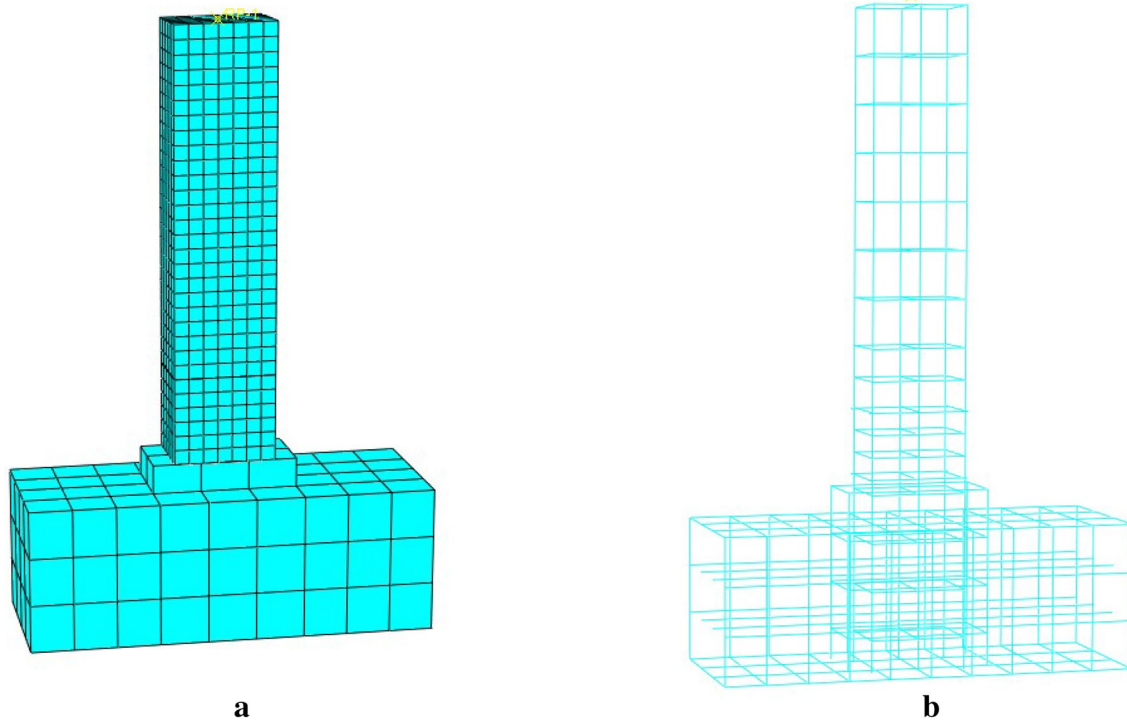


**Fig. 12** FE modeling of the precast concrete column with improved URF connection (ZP6): **a** meshed concrete; **b** the reinforcements.

Newton–Raphson method with considering the geometrical and material nonlinearity.

The damage plasticity concrete model and the William–Warnke five-parameter failure criteria in ABAQUS were used for concrete material in the models. Parameters of the constitutive model, including the elastic modulus ( $E_c$ ), dilation angle, eccentricity ratio, and viscosity coefficient, were all determined according to previous researches by Ding et al. (2011, 2017). While for the steel parts, the combined hardening constitutive model with Von Mises yielding criteria was applied. This model can consider the kinematic and isotropic hardening, together with the Bauschinger effect for steel under cyclic loads. The elastic modulus ( $E_s$ ) and Poisson's ratio ( $\rho$ ) were set to 206,000 N/mm<sup>2</sup> and 0.3, respectively. The yield stresses were all settled based on the tensile test results in Table 2. Value of the Kinematic hard parameter ( $C1$ ), the back-stress parameter ( $\gamma$ ), the maximum variation of the yield surface ( $Q_\infty$ ) and the hardening parameter ( $b_{iso}$ ) were settled as 7500, 50,  $0.5f_y$  and 0.1, respectively.

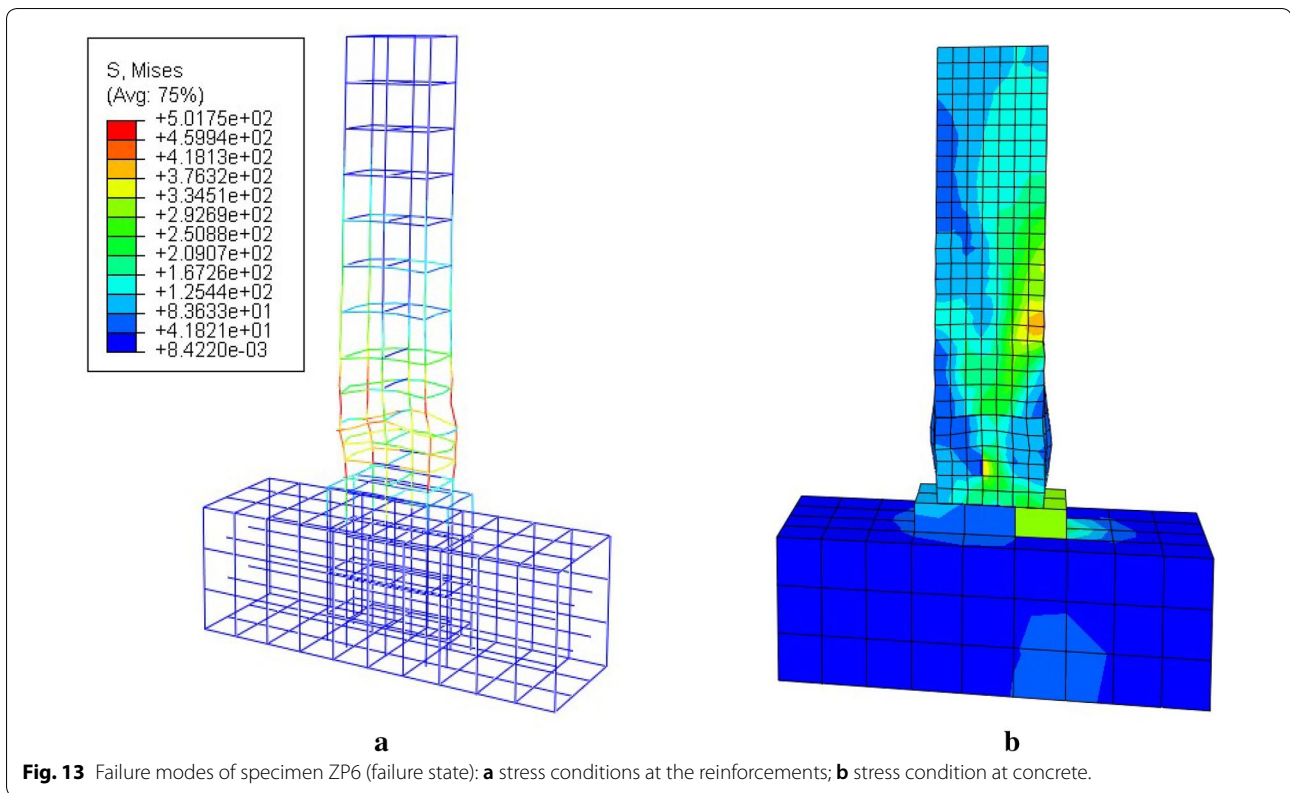
#### 4.2 Model Verification and the FEA Results

Figure 13 shows the deforming pattern and the Von Mises stress distribution at steel reinforcements and the concrete parts in specimen ZP6. At failure state, the plastic deformation of concrete parts was mainly

concentrated at the spliced region. Steel bars at the spliced region all yielded, and the local buckling deformation and the bulged-out failure were presented. Since the standard finite element analyses cannot simulate the concrete crushing, then the outward deformation was presented at the root of the concrete column, which was in fact spalled in the test. The finite element model also displayed slight stress concentration at the boundary section between precast and post-cast parts, which failure mode was similar to the observations during the test. Figure 14 gives the comparison of load–displacement relations of the specimen BASE, ZP1 and ZP6 between test data and the numerical results. Good agreements were achieved with basically consistency strength development and similar degradation process with the test data. Therefore, the effectiveness of the finite element models was verified and the FEA models can be used for further investigations.

#### 4.3 Damage Analysis of the Concrete

The tested columns displayed accumulated concrete damage, and the damage extent was intense as the number of loading cycles increased. In the numerical simulations, the damage extent of the concrete could be reflected from the DAMAGET index in Abaqus. According to references (Hibbett et al. 1998), a high value of DAMAGET



represents more severe damage in the column concrete. Figure 15 shows the plastic damage development of specimen ZP6 at different states. At the cracking stage, ZP6 already presented slight concrete damage at the root of the column. Then, as the loading amplitude increased, the damage region continuously extended up. At the ultimate state and the failure state, the high DAMAGET (larger than 0.9) region almost reached the mid-height of the column, indicating the spread of the damage pattern in specimen ZP6. This concrete damage distribution was consistent with the crack distribution in Fig. 5, that the cracks not only were concentrated within the 300 mm postcast region but were also spreading along the lower half range of the column. This damage distribution and failure mode indicated a firm connection and good integrity of the PC column.

#### 4.4 Parametric Study

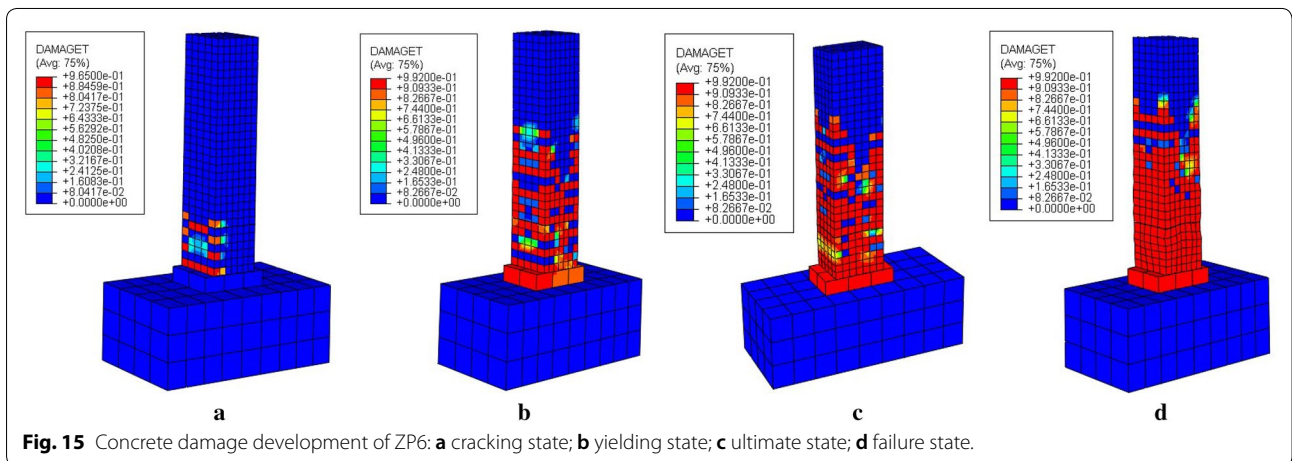
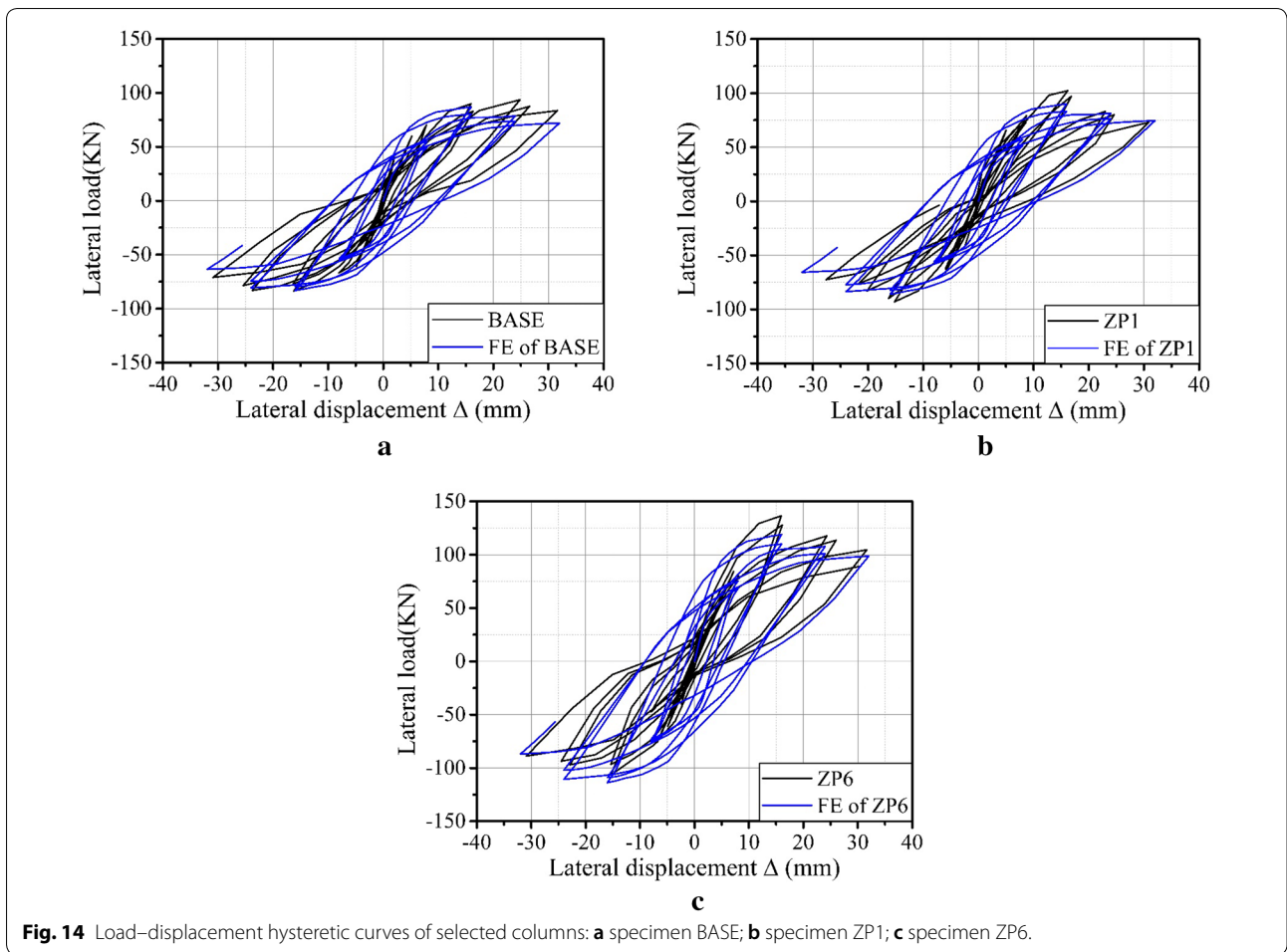
To further understand the performance of the PC columns connected with the modified fully welded URF connection, a simple parametric study was conducted on the basis of the FEA model for specimen ZP6. The investigated factors were the axial load ratio and the strength of the postcast concrete. The selected axial compression ratio ranged from 0.3 to 0.6, and the strength of the postcast concrete varied from C30 to C45. Figures 16 and 17

compare the specimens under various axial compression ratios and postcast concrete strengths. As the axial load increased, the lateral resistance of the PC column slightly increased. Furthermore, as the strength of the postcast concrete increased, the lateral strength development of the PC column also increased, especially around the ultimate strength states. Reasons for the improvement were that the high-strength concrete in the postcasting area can provide strong resistance and postpone the concrete failure at the column root. Then, the lateral bearing strength of the PC column was higher. However, the improving effect of the axial compression ratio and the concrete strength at the postcast region was limited.

#### 5 Conclusions

This paper proposed a modified U-type reinforcement ferrule connection, and the connection performance and optimum design were investigated through quasi-static cyclic tests and FEA simulations. The following conclusions were drawn:

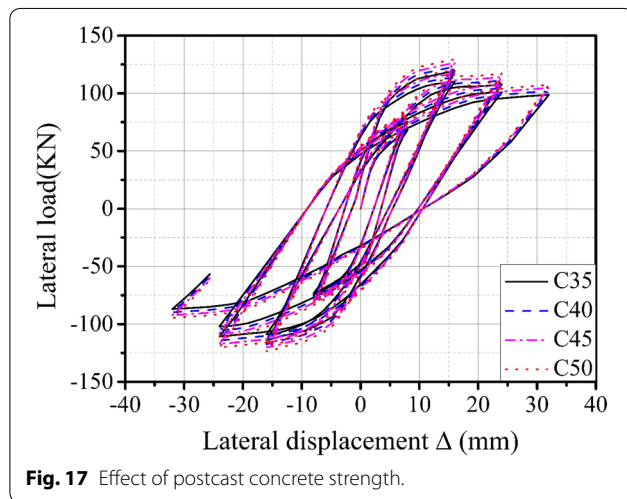
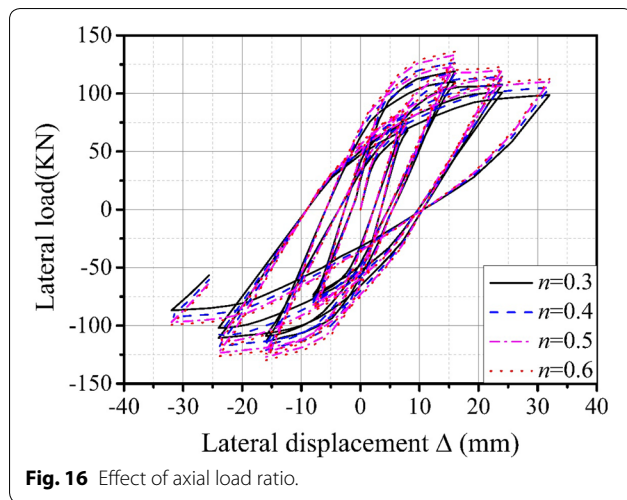
The improved URF connection improved the bonding of the reinforcement through welding of the U-ferrules. The test results indicated that the columns with the improved URF connection displayed better lateral strength and ductility performance than the column with the previous URF connection and the CIP column.



Columns with the full-length welded URF connection and spliced-sleeve connection displayed an evenly distributed cracking mode. The nonwelded or limited-length welded specimens displayed more through cracks

at the boundary levels between the PC parts and the postcast region.

From the point of view of load bearing capacity, ductility performance, stiffness degradation and energy



dissipation ability, the fully welded and the 15d identical-welded URF connections can provide a reasonable connecting ability, with a connecting ability being similar to that of the spliced-sleeve connection and better than that of the CIP column.

The increase in the axial load ratio and the concrete strength in the postcast region had a slight improving effect on the lateral resistance, but this improving influence was limited.

#### Authors' contributions

ZY and FD are in charge of the research plan; XL and XP are in charge of the experimental work; YY is in charge of the FE simulations and the paper writing. All authors contributed to write the paper. All authors read and approved the final manuscript.

#### Funding

This research work was financially supported by the National Natural Science Foundation of China, Grant No. 51708402, and the National Key R&D Program, Grant No. 2017YFC0703404.

#### Availability of data and materials

The data in the paper will be supplied upon request.

#### Competing interests

The authors declare that they have no competing interests.

#### Author details

<sup>1</sup> School of Civil Engineering, Central South University, Changsha 410075, China. <sup>2</sup> National Engineering Laboratory for High Speed Railway Construction, Changsha 410075, China. <sup>3</sup> Engineering Technology Research Center for Prefabricated Construction Industrialization of Hunan Province, Changsha 410075, People's Republic of China.

Received: 27 April 2019 Accepted: 24 August 2019

Published online: 11 November 2019

#### References

- Belleri, A., & Riva, P. (2012). Seismic performance and retrofit of precast concrete grouted sleeve connections. *PCI Journal*, *57*, 97–109.
- Choi, H.-K., Choi, Y.-C., & Choi, C.-S. (2013). Development and testing of precast concrete beam-to-column connections. *Engineering Structures*, *56*, 1820–1835.
- Ding, F.-X., Yin, G.-A., Wang, L.-P., Hu, D., & Chen, G.-Q. (2017). Seismic performance of a non-through-core concrete between concrete-filled steel tubular columns and reinforced concrete beams. *Thin-Walled Structures*, *110*, 14–26.
- Ding, F., Ying, X., Zhou, L., & Yu, Z. (2011). Unified calculation method and its application in determining the uniaxial mechanical properties of concrete. *Frontiers of Architecture and Civil Engineering in China*, *5*(3), 381.
- Elliott, K. S. (2016). *Precast concrete structures*. Boca Raton: CRC Press.
- Ghaye, H. H., Razak, H. A., & Sulong, H. R. (2017). Development and testing of hybrid precast concrete beam-to-column connections under cyclic loading. *Construction and Building Materials*, *151*, 258–278.
- Gulkan, P. (1998). *The Ceyhan-Misis earthquake of 27 June 1998: A preliminary engineering reconnaissance report*. Ankara: Implementation and Research Center.
- Hibbett, Karlsson, & Sorensen, (1998). *ABAQUS/standard: User's manual*. Providence: Hibbett, Karlsson & Sorensen.
- Hu, J. Y., Hong, W. K., & Park, S. C. (2017). Experimental investigation of precast concrete based dry mechanical column–column joints for precast concrete frames. *The Structural Design of Tall and Special Buildings*, *26*(5), e1337.
- JGJ/T101-2015. (2015). *Specification for seismic test of buildings*. Beijing: China Architecture & Building Press. (In Chinese).
- JGJ1-2014. (2014). *Technical specification for precast concrete structures*. Beijing: China Architecture & Building Press. (In Chinese).
- José, R. A., Carlos, A. B., José, I. R., & Fabio, C. (2018). Seismic performance of precast concrete column-to-column lap-splice connections. *Engineering Structures*, *172*, 687–699.
- Kim, M. S., & Lee, Y. H. (2019). Structural behavior of spliced post-tensioned girders with precast box segments. *International Journal of Concrete Structures and Materials*, *13*(1), 21.
- Mitchell, D., DeVall, R. H., Saatcioglu, M., Simpson, R., Tinawi, R., & Tremblay, R. (1995). Damage to concrete structures due to the 1994 Northridge earthquake. *Canadian Journal of Civil Engineering*, *22*(2), 361–377.
- Nzabonimpa, J., & Hong, W.-K. (2018). Structural performance of detachable precast composite column joints with mechanical metal plates. *Engineering Structures*, *160*, 366–382.
- Ou, Y.-C., Wang, P.-H., Tsai, M.-S., Chang, K.-C., & Lee, G. C. (2009). Large-scale experimental study of precast segmental unbonded posttensioned concrete bridge columns for seismic regions. *Journal of Structural Engineering*, *136*(3), 255–264.

- Park, R. (2002). Seismic design and construction of precast concrete buildings in New Zealand. *PCI Journal*, 47(5), 60–75.
- Park, S.-C., Hong, W.-K., Kim, S., & Wang, X. (2014). Mathematical model of hybrid precast gravity frames for smart construction and engineering. *Mathematical Problems in Engineering*. <https://doi.org/10.1155/2014/916951>.
- Sayadi, A. A., Rahman, A. B. A., Jumaat, M. Z. B., Alengaram, U. J., & Ahmad, S. (2014). The relationship between interlocking mechanism and bond strength in elastic and inelastic segment of splice sleeve. *Construction and Building Materials*, 55, 227–237.
- Sayadi, A. A., Rahman, A. B. A., Sayadi, A., Bahmani, M., & Shahryari, L. (2015). Effectiveness of elastic and inelastic zone on behavior of glass fiber reinforced polymer splice sleeve. *Construction and Building Materials*, 80, 38–47.
- Smith, B. J., Kurama, Y. C., & McGinnis, M. J. (2010). Design and measured behavior of a hybrid precast concrete wall specimen for seismic regions. *Journal of Structural Engineering*, 137(10), 1052–1062.
- Smith, B. J., Kurama, Y. C., & McGinnis, M. J. (2012). Behavior of precast concrete shear walls for seismic regions: Comparison of hybrid and emulative specimens. *Journal of Structural Engineering*, 139(11), 1917–1927.
- Tullini, N., & Minghini, F. (2016). Grouted sleeve connections used in precast reinforced concrete construction—Experimental investigation of a column-to-column joint. *Engineering Structures*, 127, 784–803.
- Wu, D., Liang, S., Guo, Z., Zhu, X., & Fu, Q. (2016). The development and experimental test of a new pore-forming grouted precast shear wall connector. *KSCE Journal of Civil Engineering*, 20(4), 1462–1472.
- Yu, Z., Peng, X., Guo, W., & Peng, M. (2015a). New node connection mode and seismic performance of precast concrete shear wall structure. *Journal of Xi'an University of Architecture & Technology (Natural Science Edition)*, 47(2), 160–191. **(In Chinese)**.
- Yu, Z., Peng, X., Guo, W., & Peng, M. (2015b). Seismic performance of precast concrete shear wall with U-type reinforcements ferrule connection. *Journal of Zhejiang University (Engineering Science)*, 49, 975–984. **(In Chinese)**.

### Publisher's Note

Springer Nature remains neutral with regard to jurisdictional claims in published maps and institutional affiliations.

Submit your manuscript to a SpringerOpen<sup>®</sup> journal and benefit from:

- Convenient online submission
- Rigorous peer review
- Open access: articles freely available online
- High visibility within the field
- Retaining the copyright to your article

---

Submit your next manuscript at ► [springeropen.com](https://www.springeropen.com)

---